Supplementary 1

Land-use processing.

We reclassify NALCMS 2015 (North American Land Change Monitoring System) land-use classification to MODIS IGBP (International Geosphere-Biosphere Programme) classes already present in WRF following Table S1. NALCMS 2015 dataset subject to river channel masking, derived from topographical maps (e.g. Fernando et al. 2001). Valley floors replaced with water despite the braided river systems and outwash plains present, and hence is insufficient for our approach to simulate emissions from erodible deposits. Further complicated with the large hydrological variability in these valleys, and the recent exposure of the A'äy Chu delta following hydrological reorganisation (Shugar et al. 2017). Pre-existing static datasets demonstrate not just a failure to capture seasonality but also areas that have been consistently exposed for decades. Modifications required to insert barren land where it exists in the present. We employ a water indexing approach of Feyisa et al. (2014), as detailed in Bellamy et al. (C2) to identify erodible area as a function of frequency seasonal inundation. Water conditions at the date of simulation are identified using a quality mosaic of retrievals collected during the simulation period. Due to lacking soil texture for valley deposits; either due to inappropriate resolution (0.25°) or explicit masking of channels (e.g. ISRIC SoilGrids) soil texture is prescribed to four glaciofluvial deposits ranging from very coarse (cobbles) to very fine (silts and clays). A map of soil samples used to derive soil textures for the four outwash surfaces is given in Figure S2. Soil classes in the input soil data for the valley are modified accordingly Shao (2004) implementation in WRF prescribes dedicated soil PSDs based on model soil classification (16 classes). Soil PSDs as used by the dust emission scheme are updated for the three unique soil classes (sandy loam, sand and silt). The modified lognormal distributions used to parameterise minimally- and fully-disturbed soil PSD are given in Figure S3; Figure S4 and summarised in Table S2.

Table S1. Conversion table between NALCMS and MODIS land use classifications. *denotes addition to the MODIS IGBP definitions, with characteristics largely derived from MODIS IGBP LU=16: Barren or Sparsely Vegetated.

MODIS category	MODIS description	NALCMS description	NALCMS category
1	Evergreen Needleleaf Forest	Temperature of sub-polar needleleaf forest	1
		Sub-polar taiga needleleaf forest	2
2	Evergreen Broadleaf Forest	Tropical or sub-tropical broadleaf evergreen forest	3
3	Deciduous Needleleaf Forest	Tropical or sub-tropical broadleaf deciduous forest	4
4	Deciduous Broadleaf Forest	Temperate or sub-polar broadleaf deciduous forest	5
5	Mixed Forests	Mixed forest	6
6	Closed Shrublands	Tropical or sub-tropical shrubland	7
7	Open Shrublands	Temperate or sub-polar shrubland	8
8	Woody Savannas	/	/
9	Savannas	Tropical or sub-tropical grassland	9
10	Grasslands	Temperate or sub-polar grassland	10
11	Permanent wetlands	Wetland	14
12	Croplands	Cropland	15
13	Urban and Built-Up	Urban	17
14	Cropland/natural vegetation mosaic	/	/
15	Snow and Ice	Snow and Ice	19
16	Barren or Sparsely Vegetated	Barren land	16
17	Water	Water	18
18	Wooded Tundra	Sub-polar or polar shrubland-lichen-moss	11
19	Mixed Tundra	Sub-polar or polar shrubland-lichen-moss	12
20	Barren Tundra	Sub-polar or polar barren-lichen-moss	13
30*	*Very coarse glaciofluvial deposit	/	/
31*	*Coarse glaciofluvial deposit	/	/
32*	*Fine glaciofluvial deposit	/	/
33*	*Very fine glaciofluvial deposit	/	/

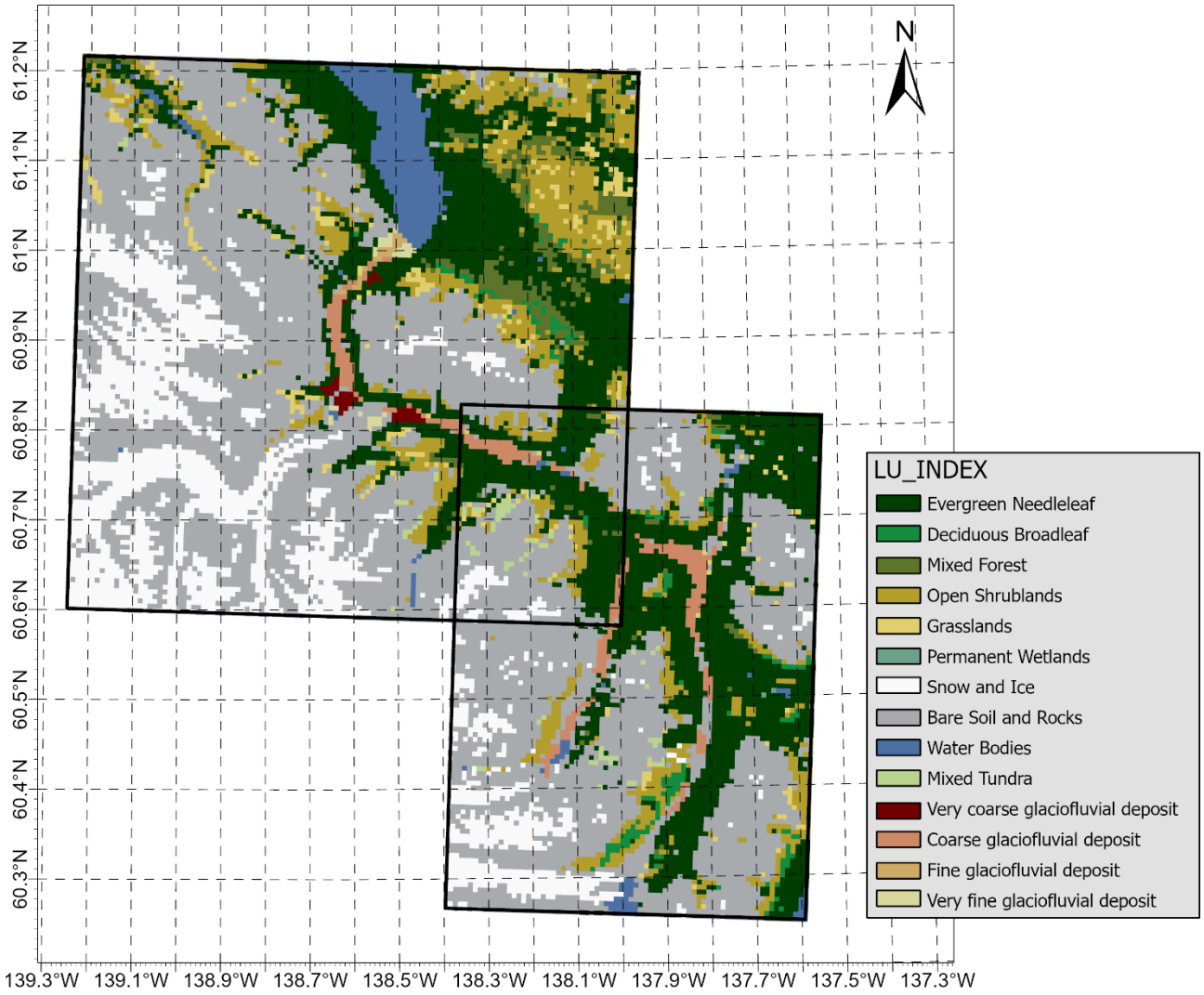

Figure S1. Example model land-use classification for d01 and d02 for September 2022 simulations.

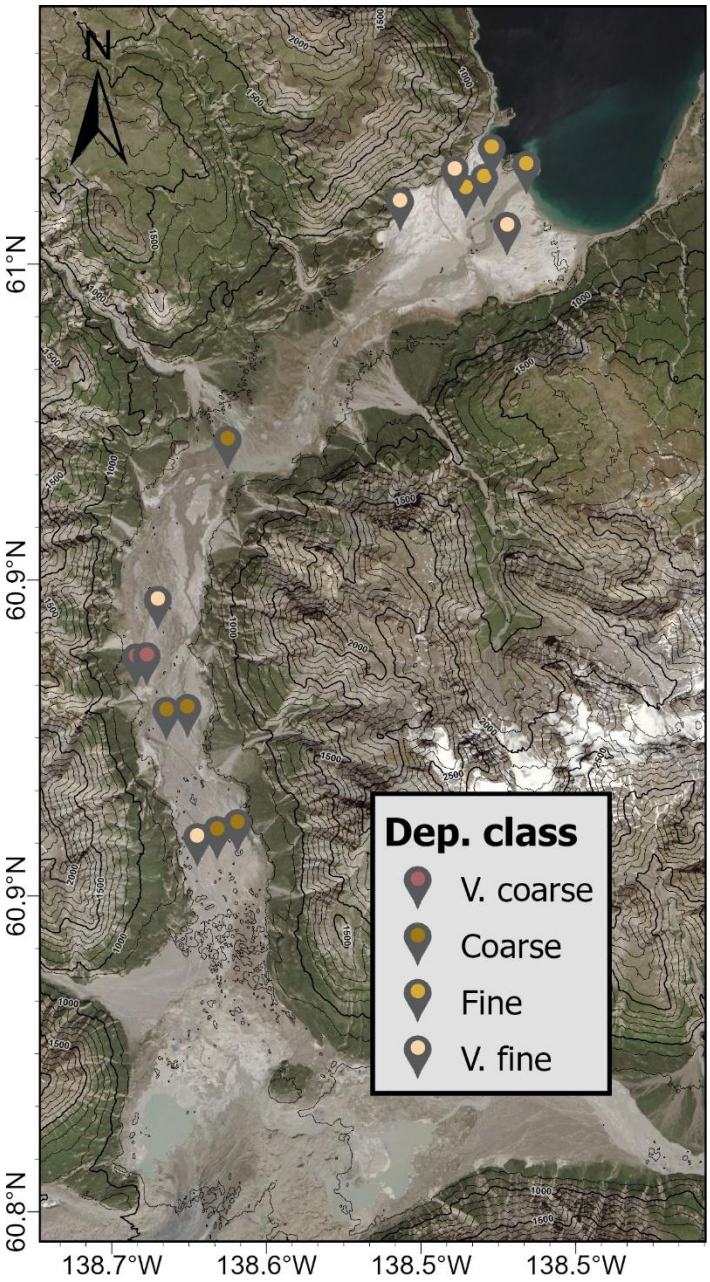

Figure S2. Soil sample locations and attribution to different glaciofluvial deposit class. Landsat 9 imagery (7 July 2023) courtesy of the U.S. Geological Survey.

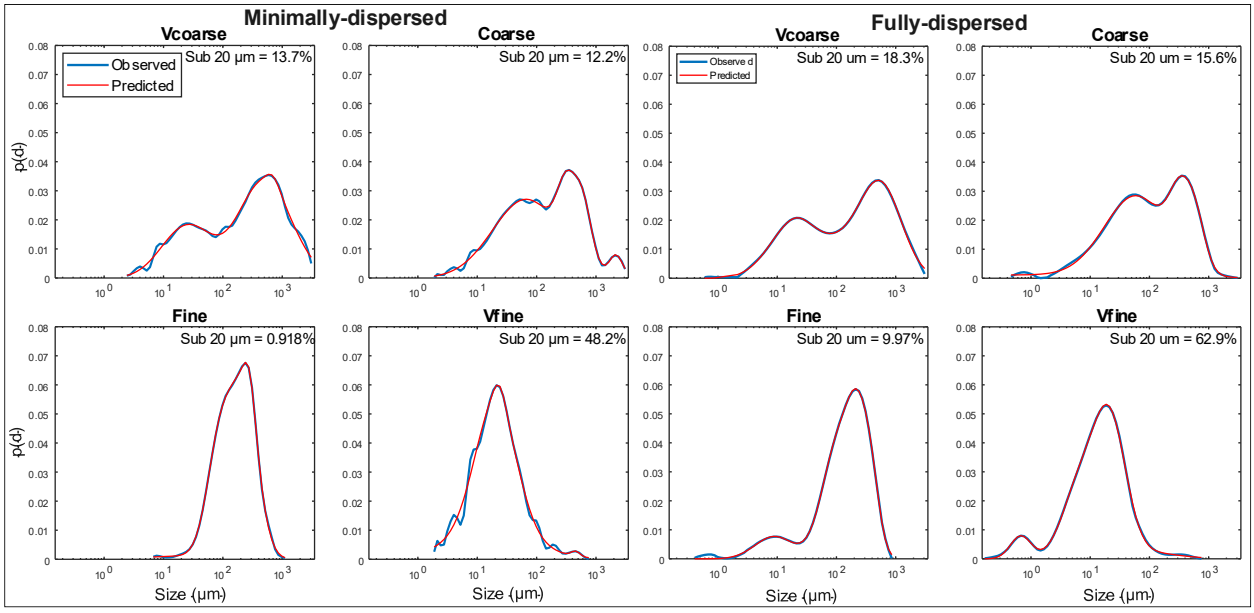

Figure S3. Minimally- and fully-disturbed particle size distributions measured (blue) and parameterised (red) introduced to the Shao (2004) scheme for this work.

Soil PSDs are represented as the sum of four lognormal modes after Shao (2004) eq(15), a frequently employed parameterisation (e.g. Gomes et al. 1990, Klose et al. 2019) for a particle size distribution ($p(d)$) of $p(d) = \frac{1}{d}\sum_{j=1}^{J}\frac{w_j}{\sqrt{2\pi\sigma_j}}\exp\left(-\frac{(ln(d)-ln(D_j)^2}{2{\sigma_j}^2}\right)$, where J is the number of lognormal modes, w_j is the mode weighting, D_j is the mode median size, σ_j is the mode standard deviation.

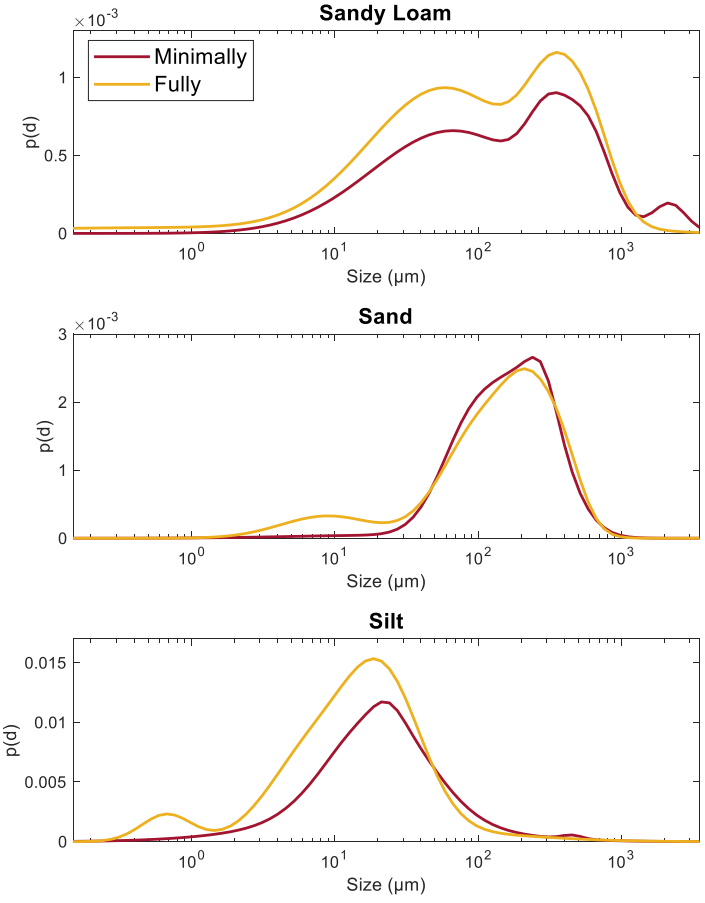

Figure S4. Minimally- and fully-disturbed (Shao et al., 2011) particle size distributions for the three modified soil classes derived from this sediment analysis in this work for outwash deposits land use classes.

Table S2. Lognormal parameters for up to four lognormal distributions parameterising soil PSDs relevant to this study.

Soil class (USDA)	Minimally (M) / Fully (F) disturbed	weight	μ (μm)	σ
Sandy loam	M	0.1365	5.8632	0.3434
		0.2706	6.5051	0.3444
		0.3414	5.9194	1.3105
		0.2514	7.7509	0.2542
	F	0.3583	5.5988	1.2330
		0.0802	11.3006	3.3949
		0.2454	6.5891	0.3596
		0.3159	6.0498	0.4497
Sand	M	0.2129	4.7765	0.5058
		0.0077	4.9271	1.3925
		0.0737	5.6976	0.2168
		0.7056	5.7294	0.5096
	F	0.0073	2.7537	0.7498
		0.3564	5.0942	0.6322
		0.1955	6.1013	0.3089
		0.4408	5.6818	0.4277
Silt	M	0.4318	5.3186	1.5869
		0.0664	6.1436	0.1686
		0.0189	3.2204	0.2383
		0.4829	3.6447	0.7909
	F	0.0017	-0.2296	0.4029
		0.3669	5.9714	1.3097
		0.1055	2.3856	0.6819
		0.5259	3.4602	0.6189

Supplementary 2

OPC data availability

OPC data availability during 2019 and 2021 is indicated in Figure S4, with missing periods highlighted. For 2019, periods of non-operation and low emission activity informed simulation period selection. For the 2021 simulation period, missing data is frequently limited to early morning periods (6 – 10 h) as a function of power supply issues and instrument maintenance.

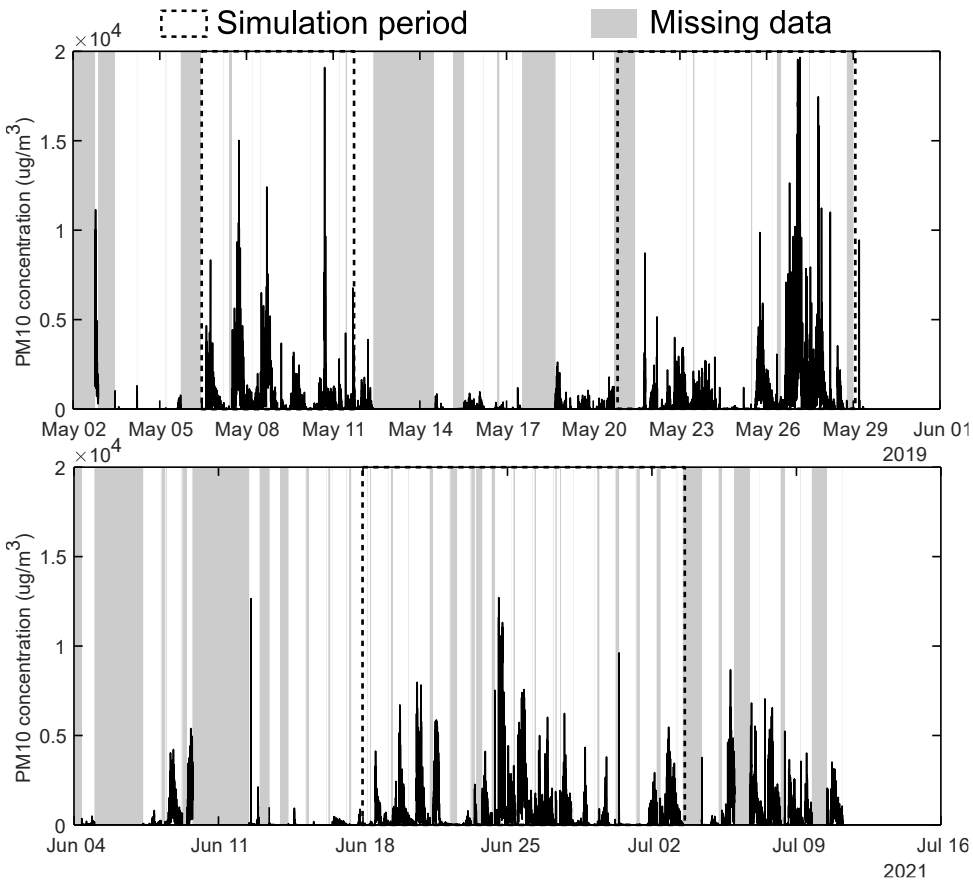

Figure S5. Available OPC measurements during May 2019 and Jun-Jul 2021, with missing data periods highlighted.

Supplementary 3

Sensitivity testing of albedo modification

In section 2.2.2 we detail modifications to prescribed albedo of the defined glaciofluvial surfaces based on albedo measurements at DV. We compare pre- and post-modification results. Agreement of both the radiative components and the associated sensible heat flux, measured independently (section 3.3.1), indicates the suitability of this change to resolve the surface energy budget at DV.

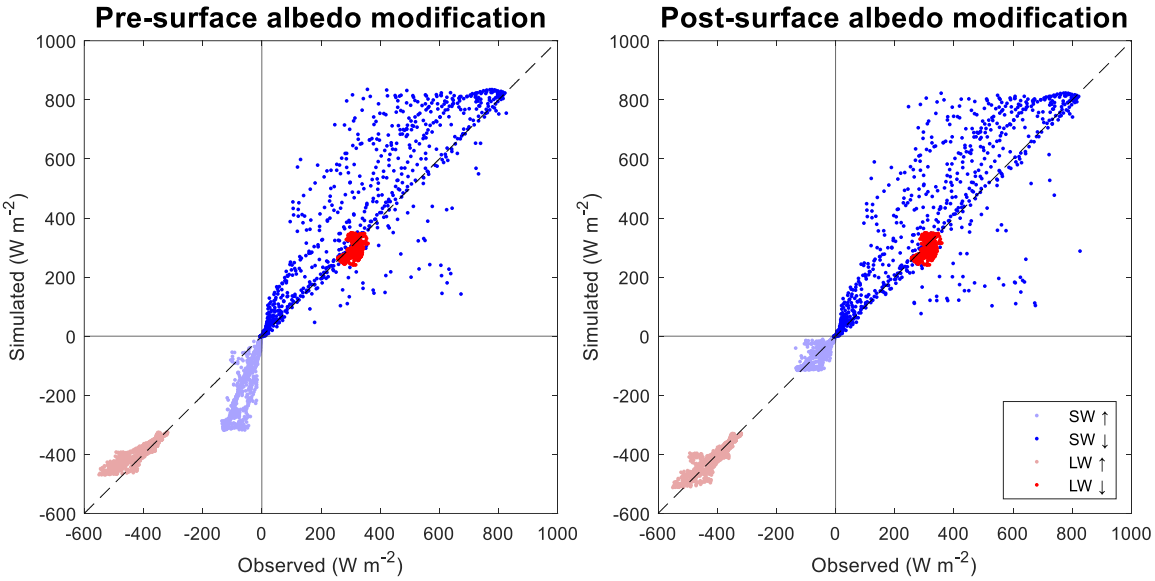

Figure S6. Pre- and post-modification influence on radiative components at DV (22 – 28 May 2019).

Table S3. Sensitivity test: simulation-period mean variables for test simulations (22 – 28 May 2019) pre- and post-albedo (α) modification for outwash deposits (lu_class=30:33).

Variable	Location	Pre-modification $\alpha = 0.38$	Post-modification $\alpha = 0.14$	% difference
Net radiation (W m^{-2})	DV	94.1	147	156
Sensible heat flux (W m^{-2})	DV	38.0	58.1	153
Surface wind (m s^{-1}) (scalar-averaged)	DV (10 m)	5.62	5.62	100
	Domain (10 m)	4.39	4.40	100
Friction velocity u_*	DV (10 m)	0.194	0.193	97
Dust emissions (metric ton) (22 – 28 May 2019)	Total	1890	2280	121
	Very coarse	0	0	100
	Coarse	1.75	2.53	145
	Fine	491	591	120
	Very fine	1390	1690	122

Supplementary 4

Deriving conversion factors for Doppler LiDAR (1.548 µm) backscatter profiles.

Doppler LiDAR-derived backscatter profiles are converted to dust mass concentrations based on the approach of Ansmann et al. (2019).

1) Input data
    a. Backscatter coefficient $\beta_d[z]$ $(Mm^{-1}sr^{-1})$ from Doppler LiDAR profiles at KLRS: May 2019.
    b. AERONET AOD (May 2019)
        i. AERONET AOD Version 3.0 Level 1.0. Extrapolated to 1.548 um based on the SDA+ algorithm (O'Neill et al., 2008; Sayedain et al., 2023) to match Doppler LiDAR wavelength.
        ii. AERONET inversion product: total concentrations (total, FM, CM) (derived product). Level 1.5 inversion product.

2) Deriving conversion factor $c_{v,d}$
    a. We extrapolate AERONET AODs to 1.548 μm: 3rd order polynomial in log AOD vs. log λ with the SDA+ algorithm (Sayedain et al., 2023).
    b. Time-match inversion-derived total volume concentration.
    c. Calculate mean extinction-to-volume conversion factor $c_{v,d}$
        i. $c_{v,d} = \frac{V_{d/D}}{\tau_d/D} = \frac{v_d}{\sigma_d}$ where V_d is the vertically-integrated particle volume concentration, τ_d is the aerosol optical depth integrated over a certain vertical extent, σ_d is the layer mean particle extinction coefficient and D is an arbitrary aerosol layer depth (1000 m as in Ansmann et al. 2019). Calculated for each viable retrieval.
        ii. Filter datasets: 1.548 μm AOD > 0.1. Due to dust source proximity, we forego the Angstrom exponent (AE) < 0.3 criteria.
3) Backscatter $\beta_d[z]$ ($Mm^{-1}sr^{-1}$) from Doppler LiDAR profiles are subsequently converted to dust mass concentration, with a LiDAR ratio $S_d = 28 \pm 3.3$ from Sayedain et al. (2023), $c_{v,d} = 0.79 \times 10^{-13}$ and particle density $\rho_d = 2650$ kg m^{-3}.
    a. Backscatter due to low-lying clouds are identified based on ground-based camera imagery and removed from analysis.

Supplementary 5

LiDAR vs. WRF vertical profile comparison: May 2019.

A full comparison of LiDAR and WRF vertical profiles at KLRS are shown in Figure S7 for the duration of simulation periods in May 2019.

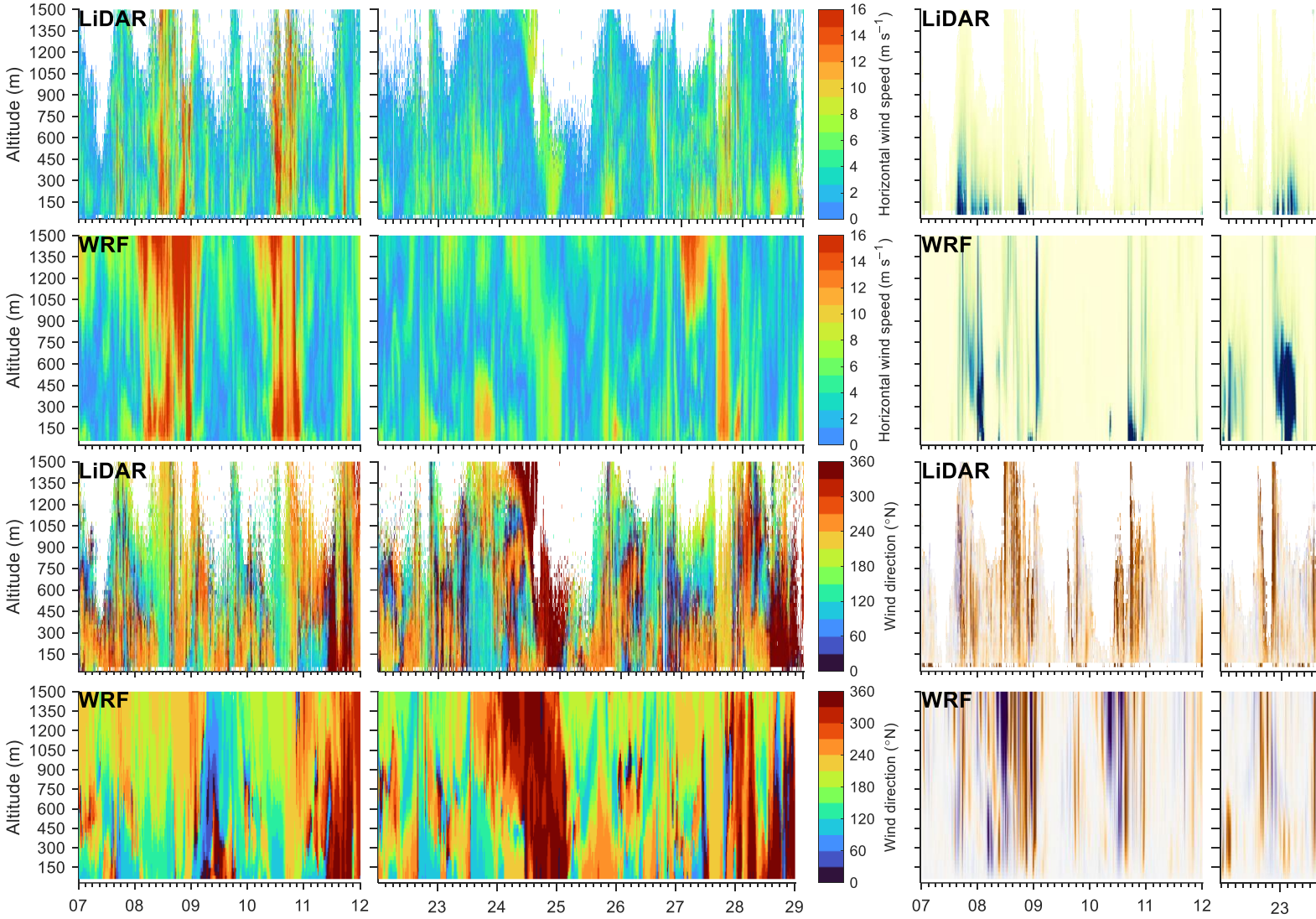

Figure S7. Comparison of LiDAR and WRF profiles at KLRS (61.027°N, 138.411°W) during simulation periods in May 2019.

Supplementary 6

700 hPa wind roses for model output during simulation periods.

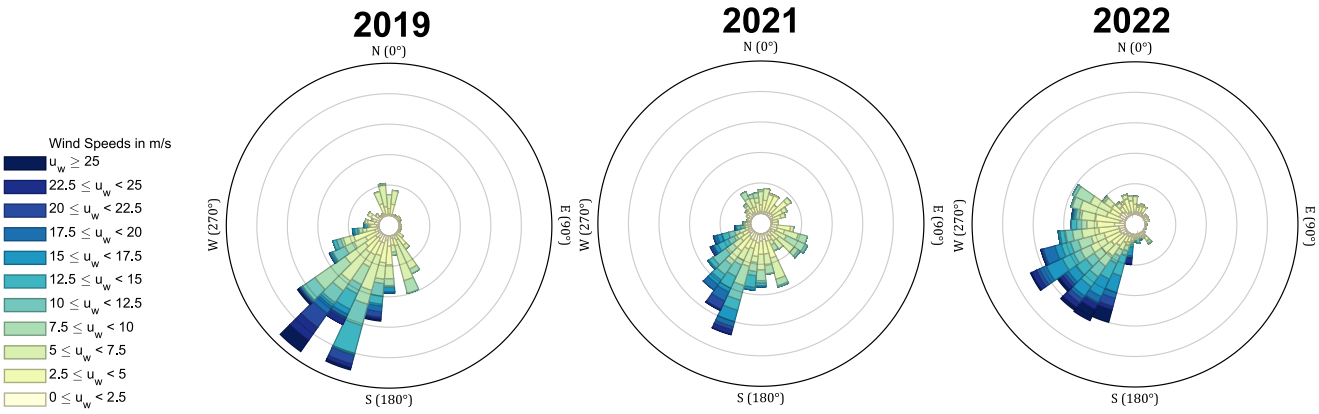

Figure S8. 700 hPa wind rose over DV (60.999°N; 138.411°W) from model output for each simulation year.

Ansmann, A., Mamouri, R. E., Hofer, J., Baars, H., Althausen, D., & Abdullaev, S. F. (2019). Dust mass, cloud condensation nuclei, and ice-nucleating particle profiling with polarization lidar: Updated POLIPHON conversion factors from global AERONET analysis. *Atmospheric Measurement Techniques*, *12*(9), 4849–4865. https://doi.org/10.5194/amt-12-4849-2019

O'Neill, N. T., Eck, T. F., Reid, J. S., Smirnov, A., & Pancrati, O. (2008). Coarse mode optical information retrievable using ultraviolet to short-wave infrared Sun photometry: Application to United Arab Emirates Unified Aerosol Experiment data. *Journal of Geophysical Research Atmospheres*, *113*(5), 1–11. https://doi.org/10.1029/2007JD009052

Sayedain, S. A., O'Neill, N. T., King, J., Hayes, P. L., Bellamy, D., Washington, R., Engelstaedter, S., Vicente-Luis, A., Bachelder, J., & Bernhard, M. (2023). Detection and analysis of Lhù'ààn Man' (Kluane Lake) dust plumes using passive and active ground-based remote sensing supported by physical surface measurements. *Atmospheric Measurement Techniques*, *16*(17), 4115–4135. https://doi.org/10.5194/amt-16-4115-2023

Shao, Y., Ishizuka, M., Mikami, M., & Leys, J. F. (2011). Parameterization of size-resolved dust emission and validation with measurements. *Journal of Geophysical Research Atmospheres*, *116*(8), 1–19. https://doi.org/10.1029/2010JD014527